Large eddy simulation of droplet breakup in turbulent flow with adaptive mesh refinement

Xiaoqiang Sun,* Hong Yan,† and Fuzhen Chen‡
Yangtze River Delta Research Institute, Northwestern Polytechnical University, Taicang, Jiangsu 215400, China
and Shaanxi Key Laboratory of Internal Aerodynamics in Aero-Engines, Xi'an 710072, China

(Received 22 February 2024; accepted 2 December 2024; published 21 February 2025)

The interaction between droplets of different scales and turbulent flow is investigated with numerical simulations. To capture the gas flow characteristics and interface evolution accurately, the large eddy simulation method is combined with adaptive mesh refinement. This numerical strategy is shown to be suitable for complex two-phase flow simulations at moderate costs. The initial sizes of droplets are the characteristic length scales in homogeneous isotropic turbulence. From large to small sizes, the finite-, inertial-, Hinze- and Taylor-scale droplets are set separately in each simulation. Results show that droplets of different initial sizes respond differently to the gas flow. Large droplets present periphery shedding at the initial stage of breakup and tend to be stretched into a disklike shape before final breakup. Small droplets are carried by the gas field and deform into cylindrical structures besides the disklike shape. Pressure perturbations are found in both phases, and the average pressure is increased on the whole. The breakup processes introduce more fine structures in the flow field, and oscillation of the energy spectra in the inertial subrange is observed. Most vorticity vectors are aligned with the second principal axis of strain rate tensor and perpendicular to the third principal axis. The distribution of vortical structures is modified by the existence of droplets, and the unstable flow patterns are found to be enhanced as droplets break up. The turbulence kinetic energy of the gas phase is suppressed more extensively with the decrease of droplet scale. The simulations provide more insights into the mechanisms of the two-phase interaction under realistic conditions.

DOI: 10.1103/PhysRevFluids.10.024004

I. INTRODUCTION

Turbulence-droplet interaction is a commonly seen phenomenon in daily life. It has significant impacts on the ecosystem as well as industrial production. For example, the breakup of ocean waves provide material and energy exchanges for creatures under the sea. The emulsion of two immiscible liquids influences the properties of chemical products. However, the mechanisms behind the two-phase interaction are far from fully understood, and most available conclusions are drawn from ideal simplified conditions. A detailed investigation from qualitative and quantitative aspects can provide insights into these complex processes.

In the application of aeroengine combustors, the interaction between droplets and turbulence is very important. Droplets of various sizes exist and interact with the pressurized inlet flow. The breakup and distribution of liquid structures can influence the combustion performance including the

*Contact author: 01sunxiaoqiang@sina.com
†Contact author: yanhong@nwpu.edu.cn
‡Contact author: chenfuzhen@nwpu.edu.cn

temperature distribution and emission level. Experiments have been largely adopted to investigate these complex phenomena. Bai *et al.* [1] conducted experiments to study the turbulent mixing of spray droplets in crossflow. They assessed the mixing degree of the droplets with a spatial parameter and found that the injection angle has more effects on the mixing of the two phases. Zhu *et al.* [2] investigated the droplet transport and dispersion in turbulent flows through experiments and obtained the spatial velocity correlations and relative velocities of droplets. Wu *et al.* [3] undertook experiments to study the turbulence modulation in air-assisted sprays. They found that the flow velocity in the gas phase was increased with the existence of droplets and that the velocity gradient and fluctuation velocity showed a segmental linear relationship.

With the development of computer capability and computational fluid dynamics (CFD), it is now possible to simulate the turbulence-droplet interaction at relatively low cost. The description of liquid phase changes from the Lagrangian particle method to dynamic interface capturing. O'Rourke [4] studied the statistical properties of droplet dispersion in turbulent flow. He derived the distribution of turbulent velocity and position changes without assumptions about the characteristic time in the flow field. Gualtieri *et al.* [5] investigated the turbulence modulation by a heavy-load suspension of particles. They showed that the energy was drained by the particles and released at small scales. The energy spectrum was modified to a new scaling law. Modeling simulations mainly focus on the macrocharacteristics of the flow field. The detailed interface deformation and effects on the whole flow field are difficult to be obtained. For the interface-capturing methods, Dodd and Ferrante [6] simulated the turbulence-droplet interaction for droplets in the Taylor scale of turbulence. They showed that the power of surface tension could be a source or sink of the two-phase turbulence kinetic energy (TKE) depending on the sign of the change rate of the total droplet surface area. Roccon *et al.* [7] investigated the influence of viscosity on breakup and coalescence of droplets in wall-bounded turbulence. They found that an increase of drop viscosity decreases the breakup rate, which can be attributed to the modulation of turbulence inside the droplet. Shao *et al.* [8] studied the effects of We number on the breakup of a droplet in emulsion process. They addressed the interaction between vortical structures and the interface. Farsoiya *et al.* [9] implemented a large ensemble of direct numerical simulations of droplet emulsion processes. They reported a breakup occurrence diagram which showed the dependence on the viscosity ratio. Detailed interface evolution and statistical flow characteristics are obtained through various numerical algorithms for two-phase flows. However, previous studies were implemented by either empirical models or an expensive direct numerical simulation method. Most studies are implemented under specific material properties and flow conditions; a systematic study of the interaction between different scale droplets and turbulence is still rare. The applicability to situations in realistic physical conditions was limited. As stated by Gorokhovski *et al.* [10] and Kim and Moin [11], additional liquid breakup scale needs to be resolved, and this scale can be smaller than the Kolmogorov scale in turbulent flow. The direct numerical simulation of complex turbulence-droplet interaction is still unreachable at current stage. To demonstrate the mechanisms of droplet breakup at the initial stage, comprehensive simulation strategies are needed.

The adaptive mesh refinement (AMR) method is naturally suitable for two-phase flow simulations and relaxes the stringent grid requirement in the whole field to resolve the interface evolution. This method automatically refines the grid to a higher resolution when the flow field changes dramatically and coarsens the grid if otherwise the flow field is smooth. Fuster *et al.* [12] studied the atomization phenomena using the adaptive octree mesh. They showed the potential of AMR to capture scales of several orders of magnitude. Agbaglah and Gilou [13] investigated the hole formation in a flapping liquid sheet with the AMR method, and the breakup mechanisms were explored with the high-resolution simulation. Although AMR has been successfully applied to two-phase simulations, published studies were mainly focused on laminar flow or materials of equal physical properties. The breakup of droplets under realistic conditions is a more complex problem. In particular, the flow field is chaotic with random velocity components when turbulence is included. In such cases, the AMR increases the grid resolution for both phases in a short time due to the rapid change of the velocity field. To avoid an unacceptable grid requirement in the

numerical simulation, it is more realistic to compute the large-scale gas motions directly and use models to account for the small-scale effects. This numerical method is called the large eddy simulation (LES) [14], and the models to represent the small-scale effect are called the subgrid-scale (SGS) models. With the combination of AMR and LES methods, it is possible to simulate realistic droplet breakup phenomena without losing accuracy for the main flow characteristics. The AMR method is responsible for capturing the detailed interface evolution, and LES is used to resolve the large-scale motions of the turbulent flow field. As suggested by Elghobashi [15], LES is used for the foreseeable future to predict turbulent multiphase flows at practical Reynolds numbers. Xiao *et al.* [16] investigated the primary breakup of a turbulent jet with LES. They found that the liquid turbulent eddies played an important role in the initial disturbing stage. Barreiro-Villaverde *et al.* [17] used LES to simulate the impinging of gas jet on a thin film. They found the dominant traveling wave in the liquid film and the most correlated flow features in the gas jet. However, there are not many studies which combine both the AMR and LES methods.

In this study we perform numerical simulations which initialize droplets of different sizes in the same turbulent gas flow field to study the turbulence-droplet interaction mechanisms. To make the two-phase simulations more applicable to complex physical conditions, the LES and the adaptive mesh refinement methods are combined in the numerical implementation. This combination has the advantage of maintaining the large-scale turbulent characteristics and possessing a high resolution on the interface. With a series of simulations, the droplet breakup processes and the effects on the overall flow field are investigated in detail.

II. NUMERICAL IMPLEMENTATION

A. Governing equations and adaptive mesh refinement method

For the incompressible gas-liquid flow, the governing equations are discretized and solved with the opensource software Basilisk [18]. It is a second-order finite volume code that coordinates accurate schemes to capture the multiphase interface flows.

The governing equations for the two phases under the Eulerian description are the continuity equation, Navier-Stokes equation, and the incompressible constraint for each phase [19],

$$\partial_t \rho + \nabla \cdot (\rho \boldsymbol{u}) = 0, \tag{1}$$

$$\rho(\partial_t \boldsymbol{u} + \boldsymbol{u} \cdot \nabla \boldsymbol{u}) = -\nabla p + \nabla \cdot (2\mu \boldsymbol{S}) + \sigma K \delta_s \boldsymbol{n}, \tag{2}$$

$$\nabla \cdot \boldsymbol{u} = 0, \tag{3}$$

where ρ is the density and the velocity vector $\boldsymbol{u}$ takes derivatives by both time and spatial coordinates in Eq. (2). p represents the static pressure and μ is the interpolated dynamic viscosity. $\boldsymbol{S} = 0.5(\partial u_j/\partial x_i + \partial u_i/\partial x_j)$ is the strain rate tensor, which represents the stretching and shearing effects. The last term on the right-hand side of Eq. (2) is the surface tension force in which the surface tension coefficient σ is set according to liquid properties. The Dirac function δ_s restricts the surface tension on the interface, and the unit normal vector $\boldsymbol{n}$ specifies the force direction. To accurately calculate the surface tension force especially when interface coalesces or breaks up, Basilisk uses an optimized height function to calculate the curvature K. This method constructs local stencils and uses finite different approximations of the derivatives of the discretized height function [19].

One prominent feature of Basilisk is its efficient and flexible adaptive mesh refinement algorithm. The quadtree/octree discretization divides a square/cubic parent grid into four or eight children grids of the same size. The conceptually simple division process facilitates the generation of high-quality grids and sets them in the relevant regions. As suggested by Popinet [18], the schemes implemented on Cartesian grids can be easily generalized to quadtree/octree discretization in Basilisk, which helps to realize the LES in the following. Readers are recommended to read the explanation of van Hooft *et al.* [20] for more details about the error-based AMR algorithm.

B. Interface capturing method

To reveal the whole process of droplet breakup in turbulent flow, the volume of fluid (VOF) [21] method is adopted in current simulations. As the name suggests, a scalar field c representing the volume fraction of the liquid/air phase in the computational grid is set and advected with the flow field. The evolution of c represents the motion of the interface. The physical variables are also weighted by c as following since the one-equation Eulerian frame is used to describe the whole flow field in the VOF method:

$$\partial_t c + \nabla \cdot (c\boldsymbol{u}) = 0, \tag{4}$$

$$\rho(c) = c\rho_l + (1-c)\rho_g, \tag{5}$$

$$\mu(c) = c\mu_l + (1-c)\mu_g. \tag{6}$$

The subscripts "g" and "l" denote the gas and liquid phases, respectively.

To reconstruct the interface on quadtree/octree mesh according to the volume fraction, the piecewise linear geometrical VOF scheme is implemented [22]. The balanced-force surface tension calculation [23] is adopted in the governing equations. The pressure correction step is carefully designed to avoid "parasitic currents" in surface tension calculation [19].

C. Large eddy simulation for two-phase flow

Large eddy simulation solves the filtered or averaged governing equations in relatively high Reynolds number (Re) flows. In LES, the large-scale three-dimensional unsteady turbulent motions are directly resolved, whereas the effects of the small-scale structures are modeled [24]. According to the Kolmogorov's secondary similarity hypothesis, which reveals the properties of turbulent flow, there exists a critical length scale ℓ_{DI} that divides the turbulent motions into two parts [24,25]. The structures larger than ℓ_{DI} are almost not influenced by the viscosity, while structures smaller than ℓ_{DI} are dominated by it. If the small-scale effects are properly treated by numerical models, simulations can reveal various large-scale motions accurately without a stringent grid requirement. In general, the discretized values on computational grids can be regarded as a kind of spatial filtered variables, and the governing equations for these filtered variables in one phase are

$$\frac{\partial \bar{u}_i}{\partial x_i} = 0, \tag{7}$$

$$\frac{\partial \bar{u}_i}{\partial t} + \frac{\partial(\overline{u_i u_j})}{\partial x_j} = -\frac{1}{\rho}\frac{\partial \bar{p}}{\partial x_i} + \nu\frac{\partial^2 \bar{u}_i}{\partial x_j^2} + F_i, \tag{8}$$

where the bar over variables represents spatial filtering, ν is the kinematic viscosity coefficient, and F_i is the body force component in the ith direction. The Einstein summation convention is applied if two same subscripts appear in a expression.

In Eq. (8) the filtered term $(\overline{u_i u_j})$ is unknown in computation. Decomposing this term as $\overline{u_i u_j} = \bar{u}_i\bar{u}_j + \tau_{ij}^r$, we obtain a known variable $\bar{u}_i\bar{u}_j$ and a new unknown variable τ_{ij}^r. This new variable τ_{ij}^r is called the subfilter scale (SFS) or subgrid scale (SGS) stress tensor, which needs to be modeled to close the filtered governing equations.

There are a number of SGS models to represent the residual SGS term τ_{ij}^r, including the eddy-viscosity models, similarity models, and mixed models to name a few. The most commonly applied model is the Smagorinsky model [14]. It belongs to the category of eddy-viscosity model and draws an analogy between the subgrid motions and molecular diffusion. The SGS motions can be regarded as a supplement to the molecular viscosity, and therefore a turbulent kinematic viscosity ν_t needs to be determined. Using the dimensional analysis and the concept of mixing length, ν_t is defined as [24]

$$\nu_t = (C_s\Delta)^2|\bar{S}|, \tag{9}$$

where $\Delta = (\Delta_x \Delta_y \Delta_z)^{\frac{1}{3}}$ is the effective filter width(or effective grid size). $|\bar{S}| = \sqrt{2\bar{S}_{ij}\bar{S}_{ij}}$ represents the magnitude of the filtered strain rate tensor $\boldsymbol{S}$. C_s is called the Smagorinsky coefficient or Smagorinsky-Lilly coefficient, which is identified through the energy transport balance relationship.

Lilly [26] simulated the turbulent energy exchange between large scale and dissipation scale to propose a value for the coefficient in the Smagorinsky model. However, this coefficient is not applicable to different turbulent flows. Germano *et al.* [27] and Lilly [28] proposed and modified the dynamic Smagorinsky model, which computes the coefficient with the advection of local flow field. Besides the grid filter presented above, a second, coarser spatial filter, called the "test" filter, is applied to the equation of motion [28]

$$\frac{\partial \hat{\bar{u}}_i}{\partial t} + \hat{\bar{u}}_j \frac{\partial \hat{\bar{u}}_i}{\partial x_j} + \frac{\partial \widehat{\left(\frac{\bar{p}}{\rho}\right)}}{\partial x_i} - \nu \frac{\partial^2 \hat{\bar{u}}_i}{\partial x_j^2} - \hat{\bar{F}} = \frac{\partial}{\partial x_j}(\hat{\bar{u}}_i \hat{\bar{u}}_j - \widehat{\bar{u}_i \bar{u}_j}) = \frac{\partial T_{ij}^r}{\partial x_j}, \tag{10}$$

where T_{ij}^r is called the subtest-scale (STS) stress tensor. The subgrid-scale and subtest-scale stress tensor are assumed and defined in a similar way:

$$\tau_{ij}^r - \tfrac{1}{3}\delta_{ij}\tau_{kk}^r = 2C\Delta^2|\bar{S}|\bar{S}_{ij}, \tag{11}$$

$$T_{ij}^r - \tfrac{1}{3}\delta_{ij}T_{kk}^r = 2C\hat{\Delta}^2|\hat{\bar{S}}|\hat{\bar{S}}_{ij}. \tag{12}$$

In the above two equations, C is the square of the Smagorinsky coefficient (C_s^2). δ_{ij} is the Kronecker delta function where $\delta_{ij} = 1$ if $i = j$ and $\delta_{ij} = 0$ otherwise. The second terms on the left-hand side of the above equations are used to ensure isotropic condition without shearing [28]. $\hat{\Delta}$ is called the test filter scale, which is usually twice the grid scale Δ. Subtracting the grid scale stress tensor from the subtest scale stress tensor, a term L_{ij} representing the stress effect falling between the test scale and the grid scale can be obtained, and it is resolvable in the simulation. Following the definitions of τ_{ij}^r and T_{ij}^r with the velocity components in Eq. (10), L_{ij} can be derived as

$$L_{ij} = T_{ij}^r - \hat{\tau}_{ij}^r = -\widehat{\bar{u}_i \bar{u}_j} + \hat{\bar{u}}_i \hat{\bar{u}}_j. \tag{13}$$

On the other hand, subtracting Eq. (11) from Eq. (12) leads to L_{ij} in terms of the strain rate tensor

$$L_{ij} - \tfrac{1}{3}\delta_{ij}L_{kk} = 2CM_{ij}, \tag{14}$$

where

$$M_{ij} = \hat{\Delta}^2|\hat{\bar{S}}|\hat{\bar{S}}_{ij} - \Delta^2\widehat{|\bar{S}|\bar{S}_{ij}}. \tag{15}$$

Combining Eqs. (13) and (14) and using the least squares method, the square of the Smagorinsky coefficient is obtained by

$$C = \tfrac{1}{2}\left(L_{ij}M_{ij}/M_{ij}^2\right). \tag{16}$$

This method calculates the model coefficient dynamically and shows better applicability in various simulations [29,30] and is thus implemented in the present work. Both the turbulent gas and liquid flows are solved with LES, and the grid resolution is set sufficiently high on the interface to capture the topological changes.

D. Linear-forcing method to maintain continuous turbulence

In this study we investigate the droplet breakup processes under continuous turbulence, which is frequently encountered in aeroengine combustor. Because our numerical scheme is implemented in physical space, we follow the linear-forcing method of Lundgren [31] and Rosales and Meneveau [32]. From the equation of motion for fluctuating velocity, they found that the turbulent flow can be perturbed to a steady state by a force proportional to the fluctuating velocity. The linear-forcing

TABLE I. Parameters of droplet emulsion simulation.

Properties	Value
Domain size (L^3)	$(2\pi)^3$
Grid number along each side (N)	256
Gas dynamic viscosity (μ_g)	1.782×10^{-3}
Liquid dynamic viscosity (μ_l)	1.782×10^{-3}
Gas density (ρ_g)	1.0
Liquid density (ρ_l)	1.0
Surface tension coefficient (σ)	0.0314
Drop diameter (D_0)	π
Root-mean-square velocity (u_{rms})	0.746
Energy-containing wave number (k_0)	10

term appears as a source term in the Navier-Stokes equation in the form of

$$\boldsymbol{F} = \mathscr{L}\boldsymbol{u}', \tag{17}$$

where $\boldsymbol{u}'$ is the fluctuating velocity and $\mathscr{L}$ is the linear forcing coefficient. It can be determined from the kinetic energy at stationary state and is equivalent to imposing a prescribed turnover timescale [32]. Unless otherwise specified, the linear-forcing term is only added in the gas flow in the following simulations. As stated by Rosales and Meneveau [32], the forcing in physical space is equivalent to forcing all the Fourier modes in the wave number space, which facilitates the energy transport analysis. From the evolution equation of energy spectrum, they found that most energy input appears at large scales at steady state.

III. RESULTS AND DISCUSSIONS

A. Verification of numerical method

The implementation of LES combined with adaptive mesh refinement and VOF method is verified through the emulsion process of a single droplet in homogeneous isotropic turbulence (HIT). The simulation conditions and parameters are adopted from the work of Shao *et al.* [8]. The initial velocity field is generated by prescribing the energy distribution in Fourier space and then transformed into physical space of uniform grids through inverse fast Fourier transforms (iFFTs). The initial energy spectrum has the form [8]

$$E(k) = \frac{16}{\sqrt{\pi/2}} \frac{u_{\text{rms}}^2 k^4}{k_0^5} \exp\left(-\frac{2k^2}{k_0^2}\right), \tag{18}$$

where u_{rms} is the root-mean-square (rms) velocity of the fluctuating velocity in each direction. k and k_0 represent the discrete wave numbers and the wave number that contains the most portion of the total turbulence kinetic energy, respectively. The initial velocity field corresponds to homogeneous isotropic turbulence, and the domain boundaries are periodic in three directions. The nondimensional simulation conditions are listed in Table I. Both the density and dynamic viscosity of the two phases are the same to address the effect of surface tension.

First, the LES method is verified for the single gas phase flow. The direct numerical simulation requirement $k_{\max}\eta \geqslant 1.5$ is satisfied with $N = 256^3$ grids, where $k_{\max}$ is the largest resolved frequency and η is the smallest scale of motion in turbulent flows, the Kolmogorov scale. The flow field turbulent Re number ($\text{Re}_t = \rho_g u_{\text{rms}} L/\mu_g$) under current conditions is around 2630. The LES simulations are implemented with grids of $N = 128^3$ and $N = 64^3$, respectively.

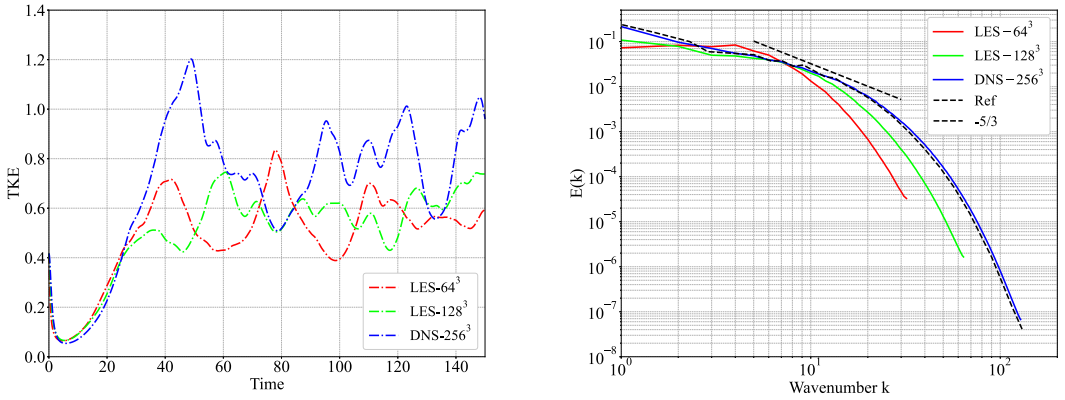

(a) TKE evolution (b) Energy spectra

FIG. 1. TKE evolution and energy spectra comparisons between LES and DNS.

Figure 1 shows the turbulence kinetic energy(TKE) evolution and the energy spectra at steady state with LES and DNS results. The turbulence kinetic energy is defined as $E_t = 1/2\rho \boldsymbol{u}'^2$ and represents the energy level contained in the fluctuating velocity of unit volume. The energy spectra represent the distribution of kinetic energy over wave numbers in Fourier space. They reveal the energy levels in different scale structures. The kinetic energy can be obtained through integration of the spectrum over wave numbers. From Fig. 1(a), it is seen that the TKE adjusts quickly at the initial stage and finally reaches a similar level of magnitude of the DNS result with the two LES simulation grids. The main portion of the energy magnitude and fluctuations are captured in the LES computations. It is seen in Fig. 1(b) that LES simulations of $N = 128^3$ and $N = 64^3$ grids capture the energy distribution well at large scales (low wave numbers). However, the energy in the intermediate range is dissipated too fast in the LES 64^3 result. With the increase of grid resolution, the turbulence kinetic energy is kept at higher magnitudes for the LES 128^3 and DNS 256^3 simulations. The energy cascade characteristic [25] is maintained using LES with $N = 128^3$ grids.

Next, the emulsion of a large droplet in homogeneous isotropic turbulence is simulated with LES and AMR methods. We first simulate the single-phase flow field to a statistically steady state of HIT and then initialize a large droplet of diameter π at the center of the flow field and investigate its breakup process. In the simulation, the highest resolution $\Delta x_G = 2\pi/256 \approx 0.0245$ is set on the interface, which is in accordance with DNS. The linear forcing is implemented in both phases with $\mathscr{L} = 0.2$. The simulation results are compared with DNS on a $N = 256^3$ uniform grid. Figure 2 shows the droplet breakup process under different resolutions for the gas phase at different times. As the grid resolution increases, finer deformation structures are seen on the liquid interface. For the LES 64^3 case, large-scale deformation is dominant, and the scale of generated droplets is relatively large. It is seen that the time sequence of the breakup process shows more similarities between LES 128^3 and DNS 256^3 simulations. The droplet deforms to a similar extent and generates similar liquid structures at the same simulation time. Both large- and small-scale deformation is seen on the interface, and the small-scale perturbations take significant effect. Although more small perturbations are captured on the interface in DNS because of the higher grid resolution in the gas phase, most of the large and intermediate scale motions are well captured with current LES and AMR combination. For the LES 128^3 case, 2353 liquid structures are generated at $T = 120$, which take up 65.2% of the liquid structures generated in DNS in three dimensions. The computation grid number for LES 128^3 case is one-fifth that of the DNS case. For the coarser LES 64^3 case, only 1512 larger liquid structures are generated.

(a) T=100.5 (b) T=102 (c) T=120

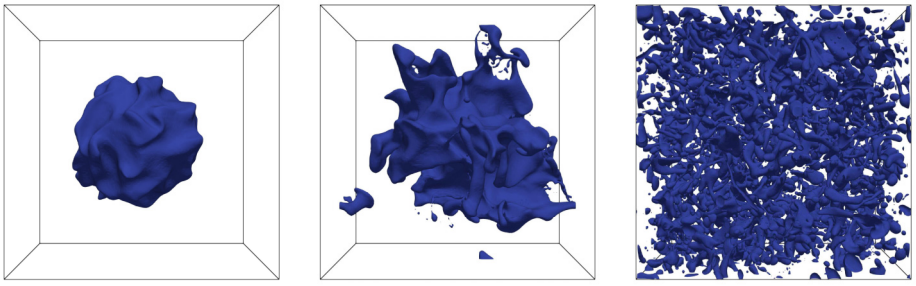

(d) T=100.5 (e) T=102 (f) T=120

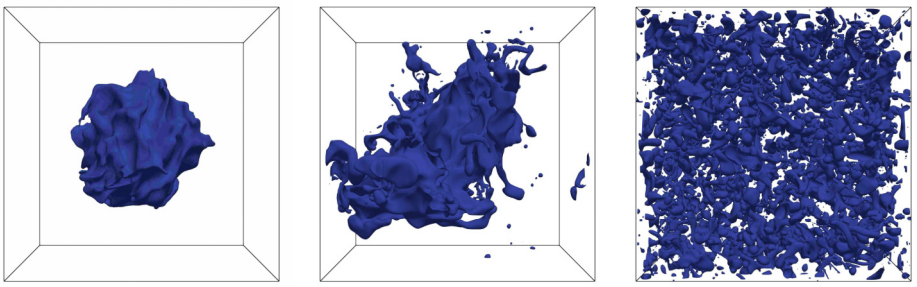

(g) T=100.5 (h) T=102 (i) T=120

FIG. 2. Comparison of interface evolution between LES and DNS. The first, second, and third rows correspond to LES 64^3, LES 128^3, and DNS 256^3 cases, respectively.

The energy spectra and compensated energy spectra of the whole flow field are presented in Fig. 3. The compensated energy is calculated as $\varepsilon^{-2/3}k^{5/3}E(k)$ according to the work of Shao *et al.* [8] Characteristic length scales can be identified with the help of this spectrum [33]. Note that the adaptive mesh refinement results are interpolated to uniform grids before the spectra calculation. Consistent results are obtained among the simulations and Ref. [8]. Large-scale energy is maintained in all simulations while the small-scale energy is dissipated and modeled in LES. Compared with the single gas phase flow [the black dashed line in Fig. 3(a)], it is observed that the small-scale energy increases due to the existence of small sized droplets, which is also observed in previous studies [6,34]. The transient compensated energy spectra in Fig. 3(b) show some oscillations, but the similar magnitude and distribution are obtained and compare well with Ref. [8] using the LES

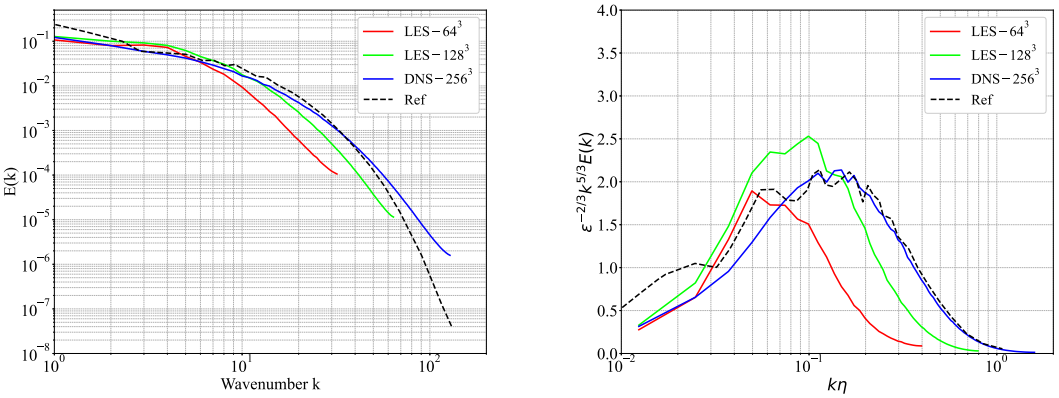

(a) Energy spectra (b) Compensated spectra

FIG. 3. Comparsion of energy spectra between LES and DNS.

128^3 grids. The combination of LES and AMR is shown to be capable of describing relatively complex two-phase flow phenomena.

B. Interaction of different scale droplets with turbulence

As stated above, droplets of different sizes exist in realistic turbulent flows. These droplets may respond differently to the flow field, and on the other hand the gas flow may be modulated by the droplets. A systematic investigation of the turbulence-droplet interaction of various scales is still rare, although some research has been carried out on the two-phase interaction of specific scales, as shown in the Introduction [6,34,35]. In this section we simulate and study the turbulence-droplet interaction under realistic conditions encountered in an aeroengine combustor with the numerical methods presented above. In each simulation, droplets of the same size which correspond to the characteristic scale in turbulent flow are set randomly in the flow field, and their response to the turbulence is investigated. The total volume fraction of the liquid phase is the same and set as 1% in each case. The turbulent flow characteristics can be set closer to realistic conditions with the LES modeling. The deformation and topological changes of the interface can be captured with high resolution using AMR and optimized VOF methods introduced. The two-phase interaction process can be obtained at a close look and analyzed with detailed flow field data. The droplet scale effect can be investigated to discover the generality and patterns at relatively low costs.

There are a few characteristic scales in realistic turbulence. From the energy and motion aspects, different length scales in turbulent flow are represented in Fig. 4 according to the classification from Pope [24]. The largest scale is the flow scale L, which represents the largest length of motion in the physical system. The next scale l_0 is the largest eddy scale (also called the "integral length scale"). As the name suggests, it manifests the length of the largest eddies in the flow field and is

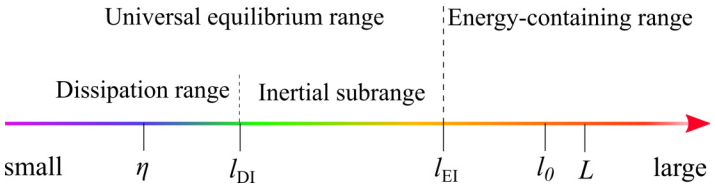

FIG. 4. Classical length scales in a turbulent flow [24].

of the same order of magnitude as L. Both the L and l_0 contain the most portion of energy in the flow field and therefore are classified as the "energy-containing scales." From Kolmogorov's second similarity hypothesis [24], there exists a middle scale range called the "inertial subrange" where the energy is transported from large scales to small scales neglecting the effect of viscous dissipation. The length scale separating the "energy-containing scales" and "inertial subrange" is represented by l_{EI}, where "E" means "energy-containing" and "I" means "inertial." The scales smaller than the inertial subrange account for almost all the viscous dissipation to keep the energy balance in the flow field. The separating scale between the inertial subrange and dissipation range is l_{DI} where "D" represents "dissipation." l_{DI} is generally close to the "Taylor scale(λ)," which is often used to characterize the grid turbulence [24]. Below the Taylor scale, motions are dominated by viscous effect, and the smallest eddy length scale, the Kolmogorov length scale η, is also in this range. Both the inertial subrange and dissipation range belong to the universal equilibrium range.

The correlations of various length scales with the integral length scale l_0 are [24,36]

$$\tfrac{1}{6} < l_{EI}/l_0 < 6, \tag{19}$$

$$\lambda/l_0 = \sqrt{10}\mathrm{Re}_t^{-0.5}, \tag{20}$$

$$\eta/l_0 = \mathrm{Re}_t^{-0.75}, \tag{21}$$

where the turbulent Re number is defined as $\mathrm{Re}_t = \rho_g u_{\mathrm{rms}} l_0/\mu_g$.

Besides the eddy scales in single gas phase flow presented above, there are also characteristic scales in the gas-liquid two phase flow. The most important length scale is the Hinze scale [37]. Hinze defined the modified Weber number (We) and used it to find the maximum droplet size which can withstand the perturbations in the statistical sense [37]. The correlation for this maximum drop diameter (Hinze scale) is

$$D_{\max} = 0.725/[(\rho_g/\sigma)^{3/5}\epsilon^{2/5}], \tag{22}$$

where ρ_g is the density of the gas phase and σ is the surface tension coefficient. ϵ represents the turbulence energy input rate, which can be substituted by the turbulence energy dissipation rate ε at steady state. Droplets of the Hinze scale are also calculated and investigated in the simulations using the correlation for energy dissipation rate [24]

$$\varepsilon \sim u_{\mathrm{rms}}^3/l_0. \tag{23}$$

The simulation domain is a triple-periodic box with $L = 0.032\,\mathrm{m}$ on each side. This size is on the order of part of an aeroengine combustor whose length scale is about 0.1 m, and the domain size is comparable to the integral length scale l_0. The reference velocity is 30 m/s, and the corresponding velocity fluctuation is set to 10% of the reference velocity according to experimental measurements [38–40]. Only the fluctuating velocity is implemented in the simulations without mean flow. The physical parameters of the two phases are set to approximate these in a combustor as much as possible, and the simulated materials are pressurized gas and liquid fuel. The turbulence in the simulation domain is homogeneous isotropic with prescribed initial velocity distribution and continuous linear forcing. Detailed simulation parameters are listed in Table II. The drop-to-gas density and viscosity ratios are 40 and 100, respectively. The surface tension coefficient of the liquid phase is close to that of kerosene fuel. Note that the nondimensional values are used in simulations and analysis.

Several characteristic length scales from large to small are estimated and used for initial droplet diameters according to Eqs. (19)–(21). The turbulent Re number is around 1.108×10^5, which is larger than similar simulations in previous studies [6,8,35]. Under such a Re number, the Kolmogorov length scale is still not resolvable and is modeled in the SGS model. The turbulence kinetic energy dissipation rate is calculated from Eq. (23) and is set to 1.0×10^{-3} to estimate the Hinze scale. Generally 10–20 grids are required to resolve the interface evolution at initial stage of breakup [11,12]. However, most droplets finally fall into the sub-Kolmogorov range under realistic working

TABLE II. Physical parameters for the gas and liquid phases.

Properties	Value	Nondimensional value
Domain size(l_0)	0.032 m	1
Reference velocity(U)	30 m/s	1
RMS velocity($u_{\rm rms}$)	3 m/s	0.1
Gas density(ρ_g)	20 kg/m^3	1
Liquid density(ρ_l)	800 kg/m^3	40
Gas dynamic viscosity (μ_g)	1.7332×10^{-5} Pa s	9.030×10^{-7}
Liquid dynamic viscosity (μ_l)	1.7332×10^{-3} Pa s	9.030×10^{-5}
Liquid surface tension coefficient (σ)	0.036 N/m	6.254×10^{-5}

conditions according to experimental measurements [15,41]. Therefore, the highest resolution is set on the interface despite that the final state of breakup is still not resolved in this study. We focus on the initial deformation and breakup processes of droplets. The volume fraction of all the droplets is around 1% in each case. The diameters of initial droplets and numbers are listed in Table III. The droplets are initialized at random positions when the single gas phase flow reaches a steady state under linear forcing. The initial condition for single-phase turbulence is prescribed by Eq. (18). The $k_0 = 2$ energy-containing wave number is adopted for the initial turbulence condition. The linear forcing coefficient $\mathscr{L}$ in the gas phase is chosen to be 0.15.

The choose of grid resolution is based on the extent of description of the flow field. Figure 5 presents the energy spectra of single-phase homogeneous isotropic turbulence field at steady state ($T=24$) as well as the resolved turbulence kinetic energy on different LES grids. We implement LES on uniform $N = 128^3$, $N = 256^3$, and $N = 512^3$ grids, respectively. From Fig. 5(a), it is shown that the classical energy spectra of HIT are recovered in the LES simulations. The LES 128^3 simulation captures the magnitude of large-scale energy, while the small-scale one is dissipated fast. The inertial subrange is not very clear. Both LES 256^3 and LES 512^3 simulations possess similar energy levels in the large-scale range, and the small-scale energy is maintained better. In the LES 512^3 implementation, the energy-containing range, inertial subrange, and dissipation range are well represented. As shown in Fig. 5(b), the difference in energy capturing decreases with the increase of grid resolution. By integrating the energy distribution over wave numbers, the resolved energy magnitude increases 17.5% from LES 128^3 to LES 256^3 grid. It further increases 3.6% from LES to LES 512^3 grid. The resolving capilibity gradually converges. To better resolve the energy transport process as well as the small-scale fluctuations, the $N = 512^3$ grid is adopted for solving the gas flow as a compromise of efficiency and accuracy. The finest grid spacing for interface capturing is $1/1024 \approx 9.766 \times 10^{-4}$, corresponding to 31.25 μm in physical units. The breakup processes as well as the interaction with the gas flow field are discussed below.

1. The overall breakup processes

The interface evolution during the breakup processes of different scale droplets is shown in Fig. 6. The initial drop sizes are the finite scale, inertial scale, Hinze scale, and Taylor scale

TABLE III. Initial droplet diameters and corresponding droplet numbers.

Characteristic range	Value	Droplet diameter	Droplet number
Finite scale	0.167	0.214	2
Inertial scale	0.01–0.167	0.08	38
Hinze scale	0.035	0.036	450
Taylor scale	0.0095	0.01	20 000

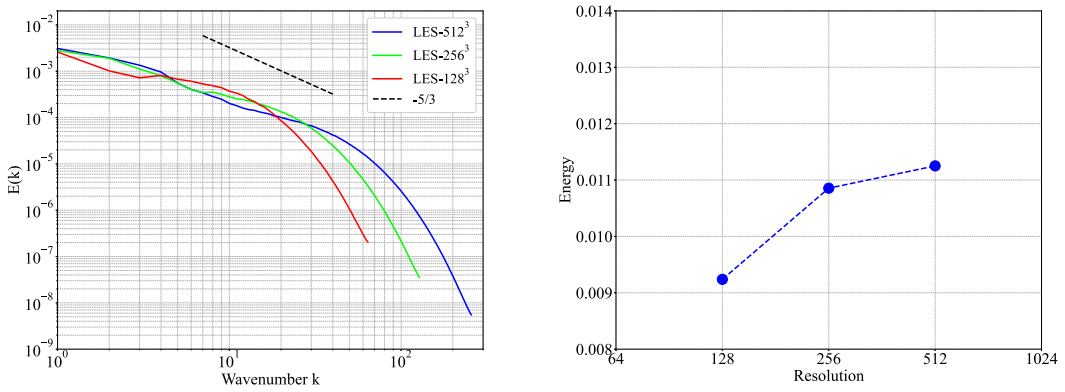

(a) Energy spectra (b) Resolved TKE magnitude

FIG. 5. Comparsion of single-phase energy spectra and resolved TKE level among different LES resolutions.

according to Table III in each simulation. Droplets break up at different rates due to the effects of inertia, surface tension, and viscous forces. Large droplets withstand the turbulent flow for longer time, and breakup happens at the location where they are initialized before very large deformation. These large droplets deform into a disklike shape before final breakup, and the general process corresponds to the "bulgy" pattern reported by Hinze [37]. The interface perturbations are obvious because of the high density and momentum of the gas phase under realistic conditions. On the other hand, the large-scale droplets also change the local gas flow field near the interface due to the high inertia. For the large-scale cases (e.g., finite scale), small droplets are first shed on the periphery of the interface. The turbulent gas flow passes the smooth droplet interface and generates liquid rims on the lee side, which are thinner in thickness and experience breakup. As the interface is stretched to a larger extent, ligaments are detached from the main droplets. Finally, the main droplets cannot hold their shapes under the continuous turbulence and experience violent breakup into fragments, ligaments, and small droplets. With the decrease of initial droplet size, the deformation process proceeds faster. The disklike shape is formed due to the shearing interaction between the two phases. For the small-scale cases, the inertia of droplets is less while surface tension becomes more significant. For the Taylor-scale case, the droplets respond quickly and are easily transported by the gas flow velocity. The small-scale perturbations and deformation are less significant and more droplets deform as a whole part. As the interaction proceeds, small-scale droplets may deform into cylindrical shape besides the disklike shape, as shown in the inset of Fig. 6(r). The deformation processes of small droplets are captured smoothly with the AMR grid resolution. When the breakup processes tend to be fully developed to reach a steady state, the probability of coalescence increases, although the volume fraction of the liquid phase is only around 1%. Some coalescence structures can be seen in the flow field, as shown in the inset of Fig. 6(t). A sequence of processes from deformation, stretching up to final breakup, can be observed in the simulation results. Finally, all cases will reach a similar state which is independent of the initial sizes.

Figure 7 demonstrates the velocity evolution on the central plane during the breakup of different size droplets. The classical random turbulent velocity profile is presented in the gas phase. From the velocity vector field, such as Figs. 7(a), 7(e), and 7(m), both large and small vortical flows are presented. These random gas flows can interact with the droplets and generate perturbations on the interface. For the largest finite-scale case, it is seen that the droplet is surrounded by high-velocity gas flow at $T = 22$. The shearing deformation is generated in the same direction with the gas flow field [Figs. 7(a) and 7(b)]. The droplet deforms irregularly in shape, and local vortical gas flow

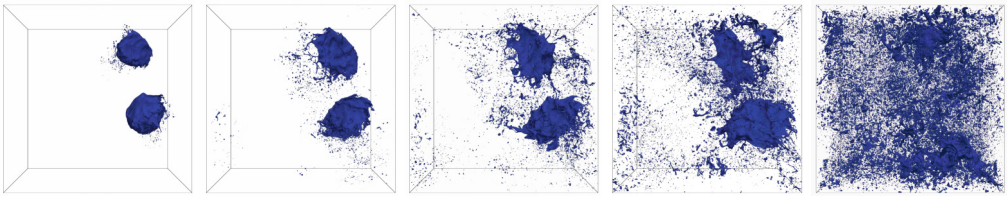

(a) $T = 22$,finite (b) $T = 24$,finite (c) $T = 26$,finite (d) $T = 28$,finite (e) $T = 36$,finite

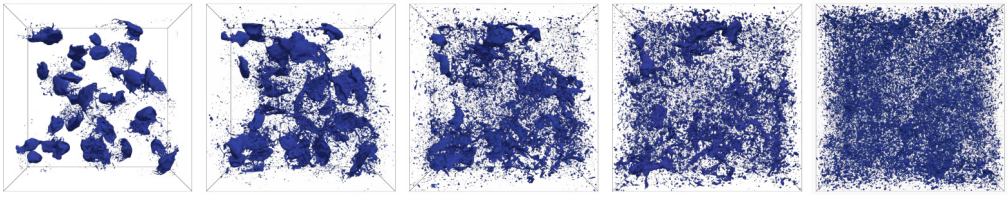

(f) $T = 22$,inertial (g) $T = 24$,inertial (h) $T = 26$,inertial (i) $T = 28$,inertial (j) $T = 36$,inertial

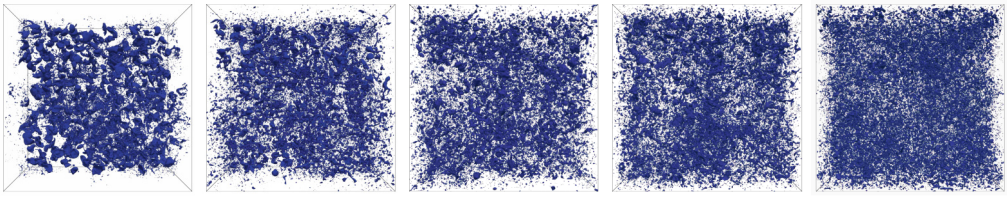

(k) $T = 22$,Hinze (l) $T = 24$,Hinze (m) $T = 26$,Hinze (n) $T = 28$,Hinze (o) $T = 36$,Hinze

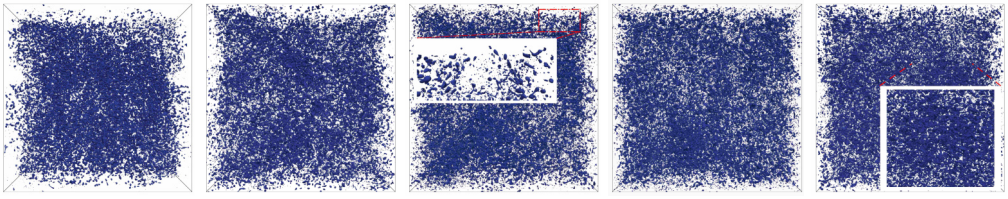

(p) $T = 22$,Taylor (q) $T = 24$,Taylor (r) $T = 26$,Taylor (s) $T = 28$,Taylor (t) $T = 36$,Taylor

FIG. 6. Breakup processes for different scale droplets.

can be generated near the interface [Figs. 7(c) and 7(d)]. The large droplet breaks up at its initial position with a very low velocity inside the liquid phase. When thin liquid sheets or ligaments are generated through interaction, higher velocity magnitude inside the droplet is observed [Figs. 7(c) and 7(f)]. The inertial- and Hinze-scale cases show similar processes with a higher deformation rate due to lower inertia. The initially stationary droplets are quickly stretched when they lie in the turbulence of high velocity and large scale [Figs. 7(f) and 7(j)]. In the breakup process of the smallest Taylor-scale droplets, it is seen that droplets quickly obtain momentum from the gas field. As the breakup proceeds, these small-scale droplets further decrease in size and follow the surrounding gas flow. The general behavior of the turbulent flow does not show much difference among different droplet scales due to the low liquid volume fraction and the continuous forcing in the flow field.

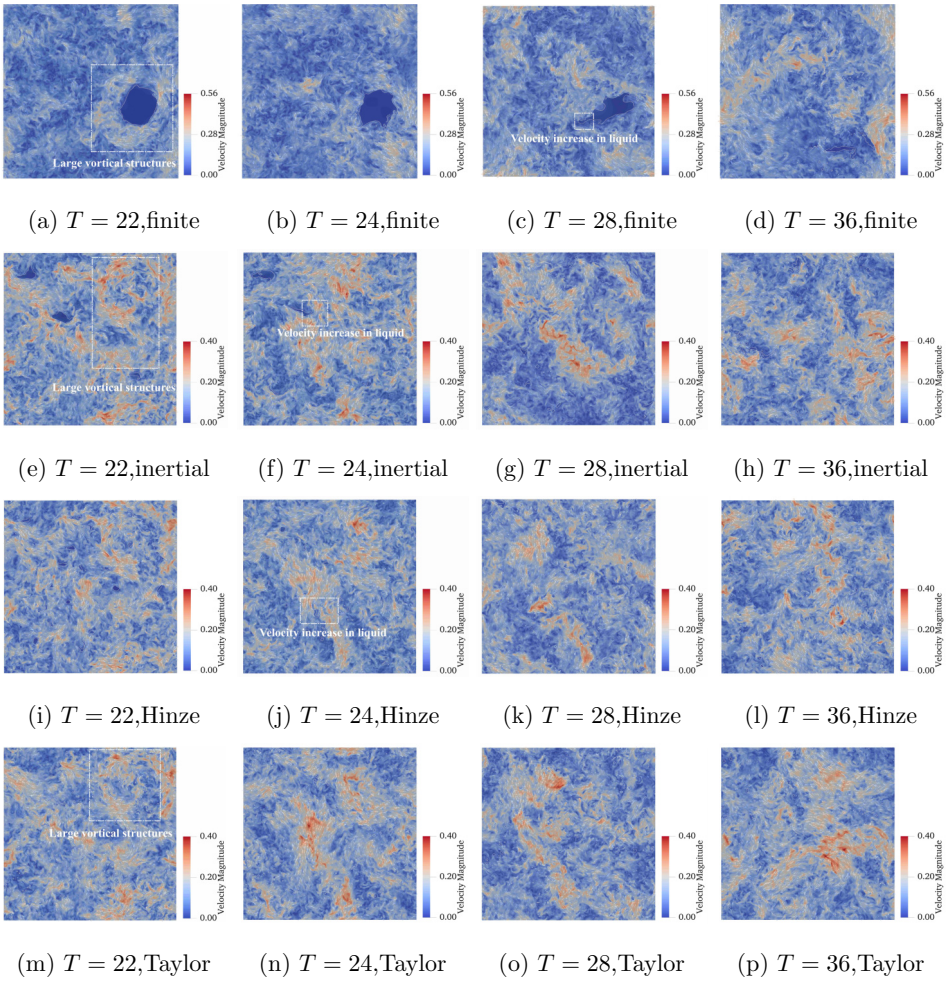

(a) $T = 22$,finite (b) $T = 24$,finite (c) $T = 28$,finite (d) $T = 36$,finite

(e) $T = 22$,inertial (f) $T = 24$,inertial (g) $T = 28$,inertial (h) $T = 36$,inertial

(i) $T = 22$,Hinze (j) $T = 24$,Hinze (k) $T = 28$,Hinze (l) $T = 36$,Hinze

(m) $T = 22$,Taylor (n) $T = 24$,Taylor (o) $T = 28$,Taylor (p) $T = 36$,Taylor

FIG. 7. Velocity contours with interface during the breakup processes.

Figure 8 shows the static pressure on the central plane in finite- and Taylor-scale cases. The detailed pressure distribution in turbulent flow as well as in different size droplets is presented with current grid resolution. The pressure field also shows random characteristics in the gas phase, and here we focus on the two-phase interacting regions. The gas-liquid interaction is more clearly seen in the finite-scale case. Pressure oscillations are observed inside the deformed droplets. As shown at $T = 24$ in the finite-scale case, the pressure increases near the interface when gas flow impacts on the droplet in the normal direction. On the other hand, the pressure decreases near the interface when gas flow shears along the droplet, which is depicted at $T = 36$. Combining the velocity vectors and pressure contours, both the Kelvin-Helmholtz (KH) and Rayleigh-Taylor (RT) instabilities are observed for liquid structures in turbulent flow. The shearing interaction generates wavy structures, and the gas impact causes deformation and recirculation on the interface. The pressure distribution inside the liquid phase may stabilize or destabilize the droplet depending on the geometric shape of the interface and the transient interaction between the two phases. Due to the small-scale and large surface tension effect for the Taylor-scale droplets, the pressure inside these droplets is relatively larger than other scales. Pressure perturbations inside the small droplets are also captured, as shown in Fig. 8(f). The inset shows the local pressure in the Taylor scale and generated tiny droplets.

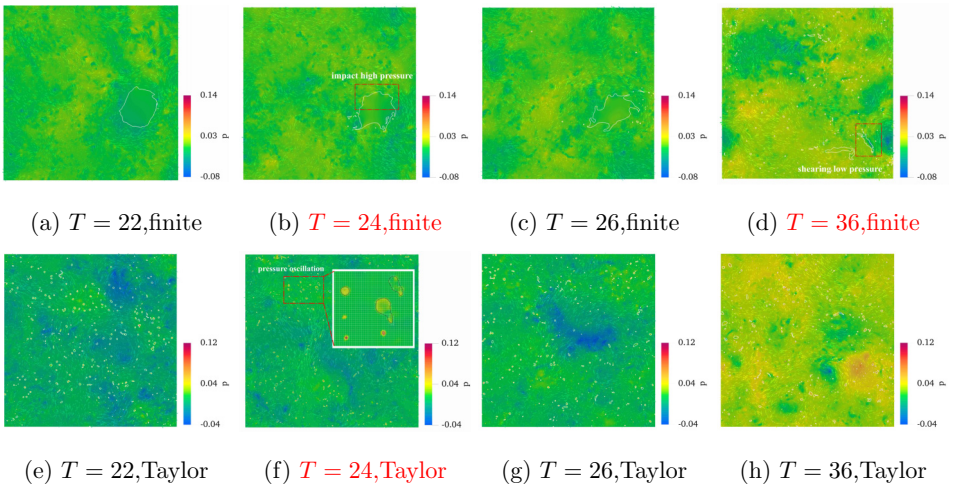

(a) $T = 22$,finite (b) $T = 24$,finite (c) $T = 26$,finite (d) $T = 36$,finite

(e) $T = 22$,Taylor (f) $T = 24$,Taylor (g) $T = 26$,Taylor (h) $T = 36$,Taylor

FIG. 8. Pressure contours with interface during the breakup process.

The corresponding AMR grid resolution is also drawn. It is seen that the shape of the Taylor-scale droplets is well captured. The shed tiny droplets possess high pressure and distribute widely in space. An interesting modification to the whole flow field is that the average pressure increases as the breakup proceeds in all simulations. For the finite-scale case, the average pressure at $T = 36$ is 16 times that at $T = 22$. For the Taylor-scale case, the average pressure increases 2.4 times from $T = 22$ to $T = 36$. This can be contributed to more fluctuations in the flow field by the existence of dispersed small droplets.

The droplet number and computational grid number with AMR implementation are generalized in Fig. 9. Droplets of all scales in our study experience further breakup under current physical conditions. The droplet number reaches a nearly steady state of around 120 000 at the end of the simulations. It is noted that resolving the whole breakup process to the sub-Kolmogorov scale is unreachable with limited computational resources. It is shown in Fig. 9(a) that the droplet number is lower for larger scale cases at initial stages due to the concentration of liquid structures and increases fast at later time under continuous perturbations from the flow field. During $T = 25$–35,

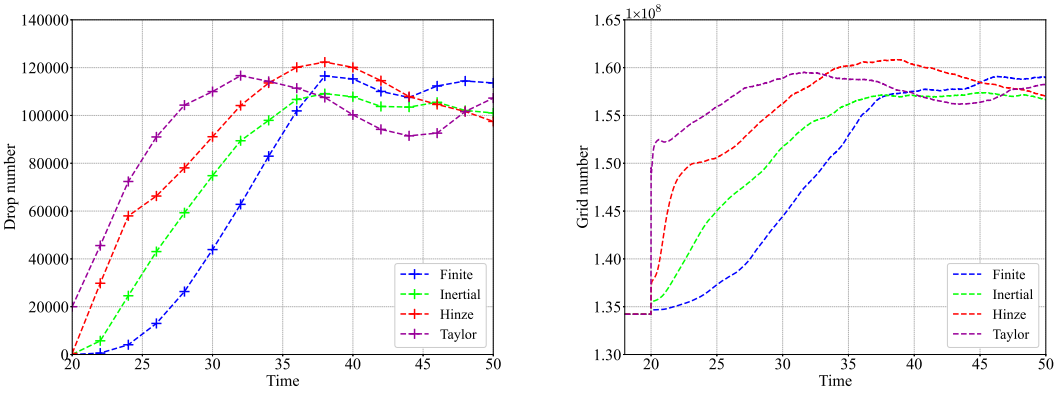

(a) Droplet number (b) Grid number

FIG. 9. Evolution of droplet and grid numbers during breakup processes.

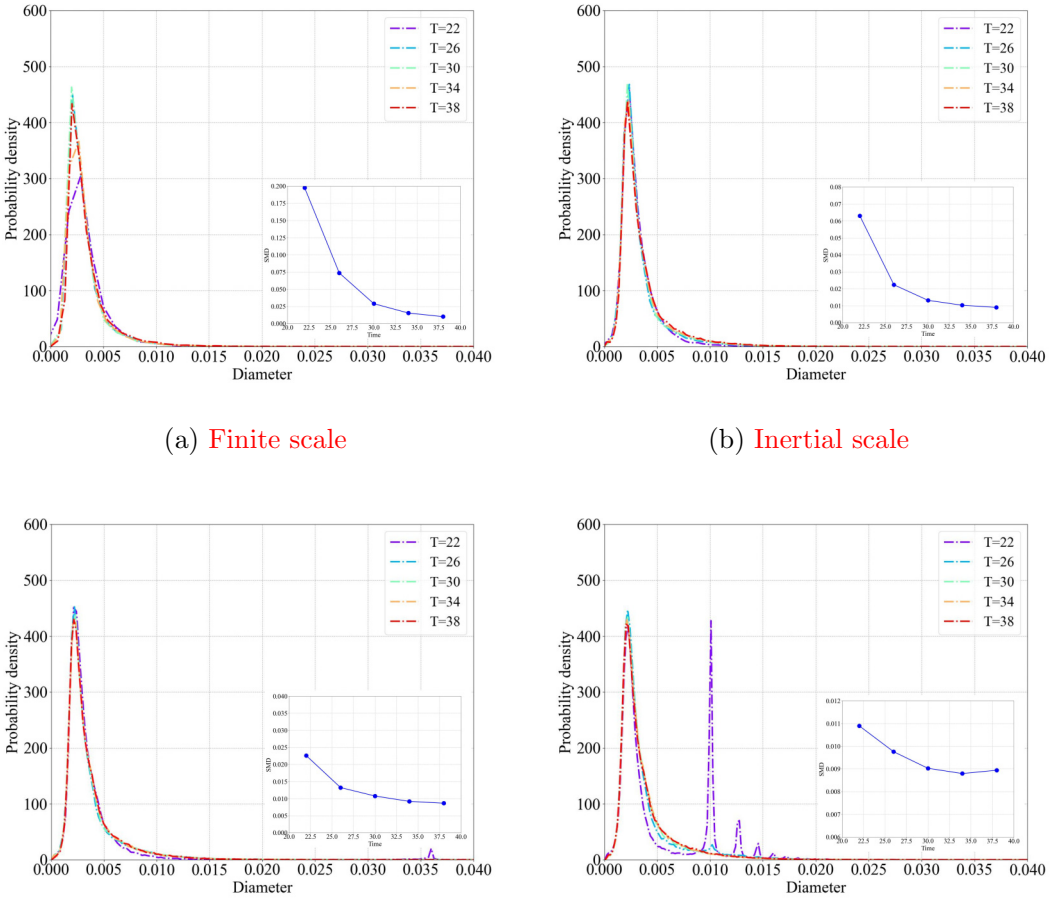

(a) Finite scale (b) Inertial scale

(c) Hinze scale (d) Taylor scale

FIG. 10. Probability density function of droplet diameter distribution.

the increase rates of different scale cases are similar. In all simulated scales, the Hinze-scale case has a large breakup rate at the initial stage, and more droplets are generated during $T = 35$–40, which manifests a strong interaction between these scale droplets and the turbulent flow. The drop numbers for the four scale cases begin to decrease due to coalescence after around $T = 40$. Finally, a balance between coalescence and breakup will be reached, which is also observed in similar investigation [34]. The grid number evolution in Fig. 9(b) shows similar trends. The more droplets exist in the flow field, the larger the computational grid number is. The grid numbers finally reach around 160 million and keep a steady level in the current study for all cases. With the increase of initial droplet scale, the steady state is reached more slowly. The current grid resolution and computational costs are acceptable to reveal the main characteristics of turbulence-droplet interaction.

The probability density function (PDF) of diameter distribution is shown in Fig. 10. The evolution of the Sauter mean diameter (SMD) which represents the average liquid diameter level is plotted as inserts (SMD $= \sum d^3 / \sum d^2$ and d is the equivalent liquid structure diameter). The main distribution characteristics show unimodal curves and are similar between different scales. Droplets whose scale is close to the grid resolution take the largest portion in the figures at different simulation time. The periphery shedding under continuous perturbed flow generates many tiny

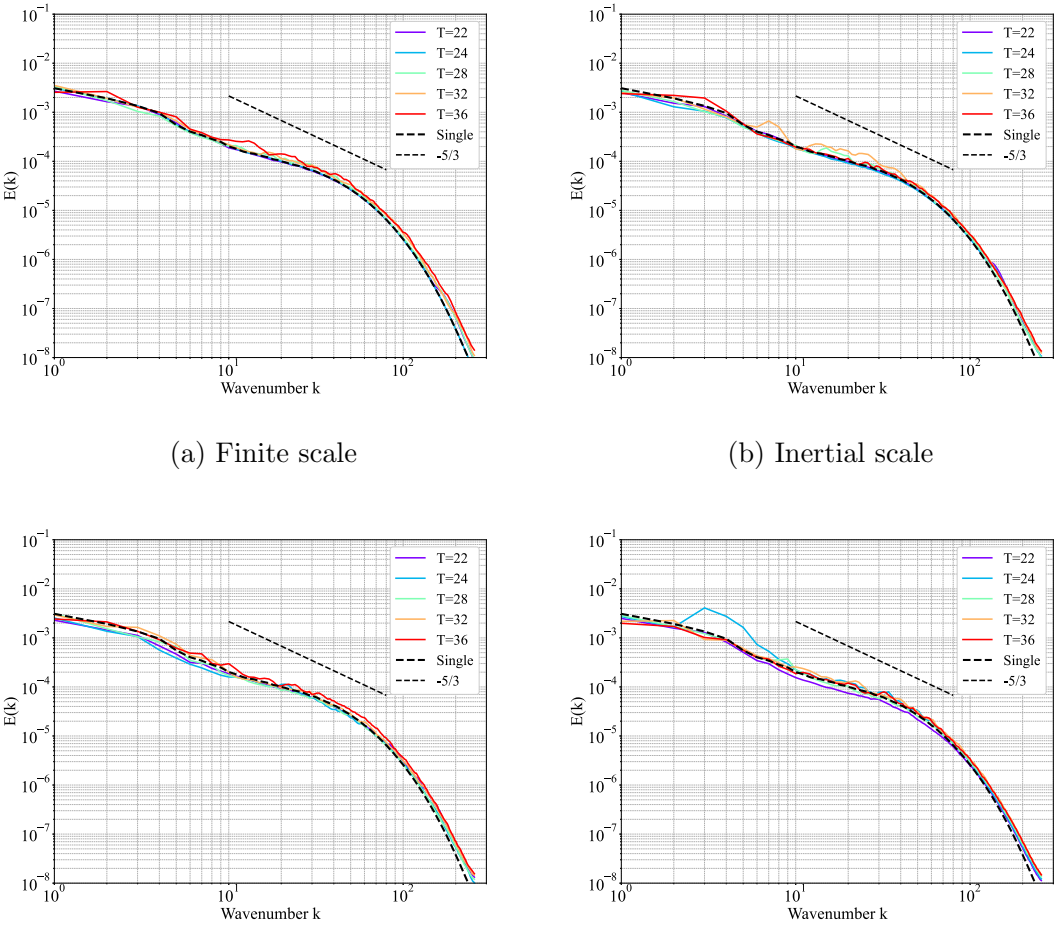

(a) Finite scale

(b) Inertial scale

(c) Hinze scale

(d) Taylor scale

FIG. 11. Energy spectra of the whole flow field in different scale cases.

droplets in all cases. The SMD level also decreases rapidly. Therefore, the probability density peak is larger at the initial stage than that at later time in simulations except the finite-scale case. For the finite-scale case, a significant increase in the curve peak due to periphery shedding is seen at initial stage of breakup. Turbulence can only shed small droplets from the main liquid structures due to the high inertia and surface tension of the liquid phase. As the breakup proceeds, a wider distribution of droplet diameter can be observed. For the Taylor-scale case, a multimodal distribution is observed at initial stage of breakup because the initial drop diameter is close to that at steady state and the initial drop number is large. It approaches the same distribution as other cases at later time. The SMD level generally changes from initial large scales to finally similar small ones among different cases to represent the breakup processes. The SMD increases to a higher value in the Taylor-scale case at $T = 38$, which shows the coalescence of droplets.

The energy spectra of the whole flow field are calculated by mapping two-phase results to a $N = 512^3$ uniform grid, as shown in Fig. 11. The energy of the liquid phase is accounted by multiplying its density. The result of single phase flow without droplets is depicted by the black dashed line, and Kolmogorov's "$-5/3$" law is also drawn. The overall spectra characteristics are similar between different scale cases and the single gas phase flow. Therefore, the spectra features are not changed

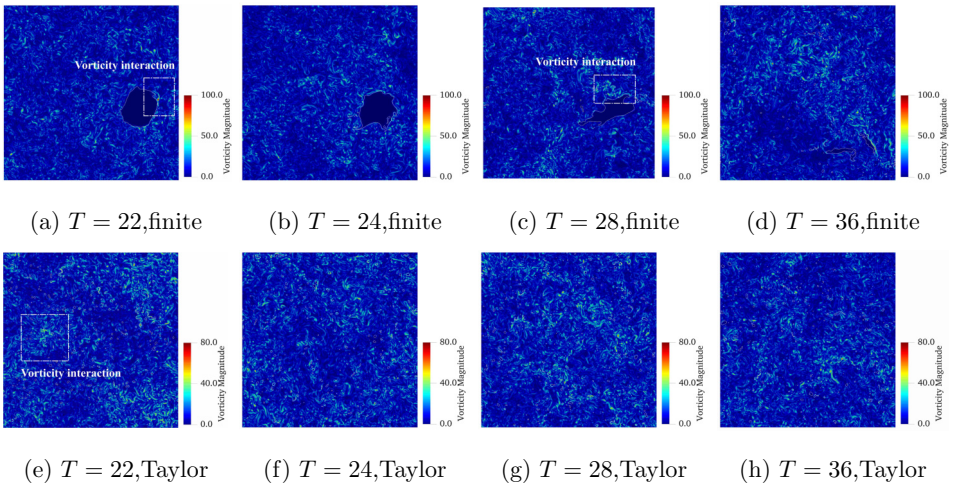

(a) $T = 22$,finite (b) $T = 24$,finite (c) $T = 28$,finite (d) $T = 36$,finite

(e) $T = 22$,Taylor (f) $T = 24$,Taylor (g) $T = 28$,Taylor (h) $T = 36$,Taylor

FIG. 12. Vorticity contours with interface during the breakup processes.

much with 1% volume fraction of the liquid phase under realistic conditions. However, the energy of the smallest scales is increased to a higher level compared with the single gas phase case in all simulations. These droplets cause the larger scale gas motions to break into smaller ones and introduce more local perturbations. For the same reason, the flow field energy is reduced in the intermediate wave numbers at initial stage for small-scale droplet cases such as the Hinze and Taylor scales, and the energy finally reaches the level of single phase flow under the linear-forcing effect. The spectra show more oscillations in the inertial wave number range due to the interaction between the two phases, and the oscillations are more significant as breakup proceeds. The energy transport process is modified to some extent with the existence of small droplets. Due to the remapping process to a relatively coarse grid, the energy in the smallest scales may be lower estimated.

2. Detailed interaction between droplets and turbulent flow

In this subsection the detailed interaction processes between droplets and turbulent flow is presented and investigated. The evolution of vortex structures is first compared under different scales. The flow patterns in the two-phase flow field are then identified. Finally, we calculate the TKE evolution of the two phases to investigate their effects on the whole flow field.

Figure 12 shows the vorticity magnitude on the central plane of the finite- and Taylor-scale cases. Vortical structures exist randomly in the gas phase and near the liquid interface. More breakup and clustering of droplets are seen in regions where large strength vortical structures lie. As shown in Figs. 12(a) and 12(c) of the finite-scale case and Fig. 12(e) of the Taylor-scale case, strong interaction between the interface and vortical structures contributes to deforming and tearing up the large droplet. Along the irregular liquid interface, local recirculating gas flow is generated. The vorticity magnitude in the liquid phase is maintained at a low level for all scales and concentrates on the interface due to its high inertia and viscosity. Therefore it is reasonable to ignore the rotational motion in the liquid phase for large droplets. However, the generated tiny scale droplets have a larger surface tension effect and can be carried by the turbulent flow, and their rotating motion can be considered and included in modeling.

To demonstrate the spatial distribution of three-dimensional vortical structures in the flow field, the Q isosurface is drawn in a specific selected region at different times in Fig. 13. $Q = 400$ is chosen to manifest vortices in the flow field where the maximum Q values in the selected region are around 4000. The majority of the Q isosurface is found in the gas flow, and it is skewed and stretched in the flow field. Most of these vortical structures are in the form of a thin cylindrical

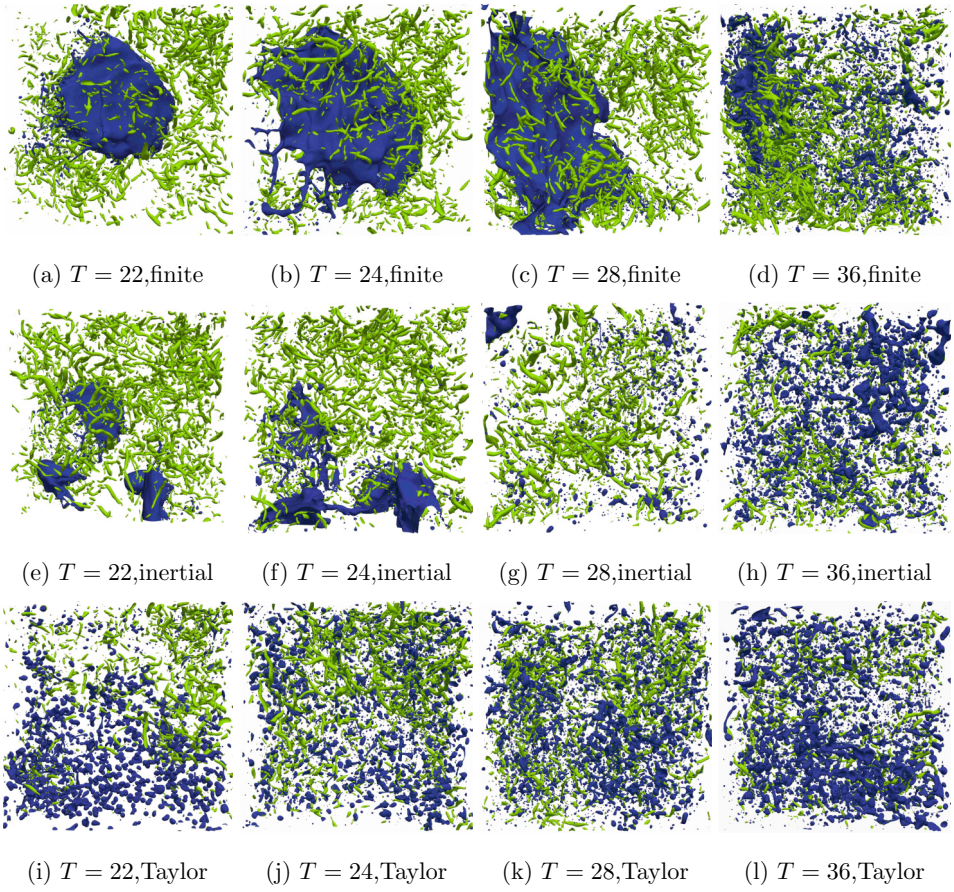

(a) $T = 22$,finite (b) $T = 24$,finite (c) $T = 28$,finite (d) $T = 36$,finite

(e) $T = 22$,inertial (f) $T = 24$,inertial (g) $T = 28$,inertial (h) $T = 36$,inertial

(i) $T = 22$,Taylor (j) $T = 24$,Taylor (k) $T = 28$,Taylor (l) $T = 36$,Taylor

FIG. 13. Q isosurface in the flow field during the breakup processes.

shape. It is interesting to find that these structures are more likely to exist in regions where the liquid volume fraction is low, as shown in Fig. 13(c) of finite scale, Fig. 13(e) of inertial scale, and Figs. 13(i) and 13(l) of Taylor scale. Therefore, the existence and breakup of droplets influence the spatial distribution of gas vortical structures. When droplets are stretched largely into thin films, the vortical structures can preserve their motions and promote the breakup of interface. As shown in Fig. 13(d) of finite scale and Figs. 13(f) and 13(h) of inertial scale, the Q isosurface structures are presented close to the liquid interface. Finally, the Q isosurface vortical structures are less seen when the dispersion level of droplets becomes high.

The PDF of the cosine of the angle between the vorticity vectors and the principle axes of strain rate tensor is plotted in Fig. 14. The principle axes of strain rate tensor are the corresponding eigenvectors. The motions are decomposed into these directions where only the axial strains take effect and the shearing ones are removed. The PDF distributions are almost identical to each other with different initial droplet scales. Most vortical structures lie in the gas phase and the influence from droplets is small. The vorticity-principle axis relationship generally follows that of single-phase gas flows [8,42]. The vorticity vectors are mainly aligned to the second principle axis $\boldsymbol{a_2}$ of the strain rate tensor where $|\cos(\theta)| = 1$. The vorticity vectors are perpendicular to the $\boldsymbol{a_3}$ axis, which represents the compressive strain rate [43]. The generation of vortical motions is promoted by the compressing effect. As droplet breakup proceeds, the perpendicularity to the third principle axis $\boldsymbol{a_3}$ is reduced to some extent.

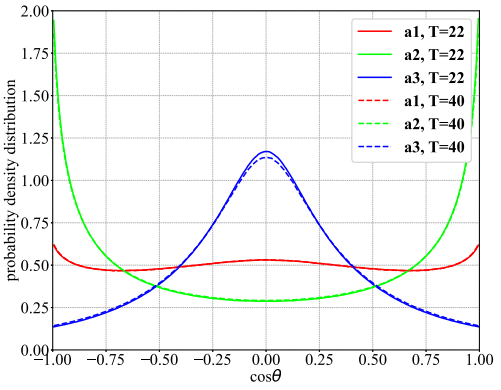

(a) Finite scale

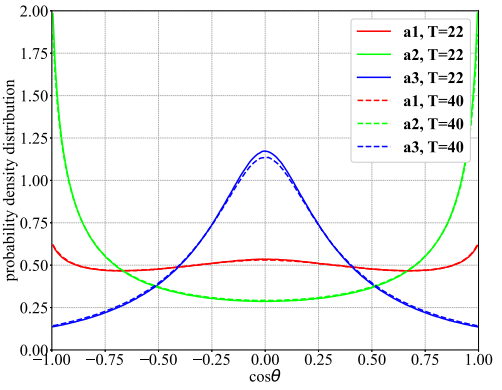

(b) Inertial scale

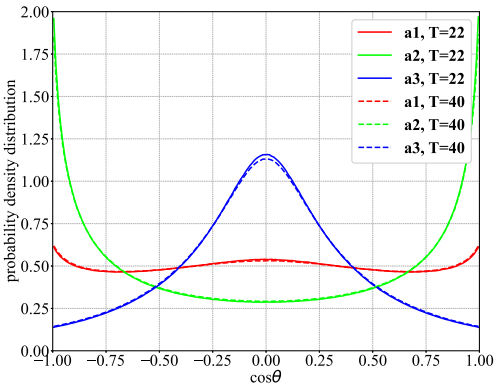

(c) Hinze scale

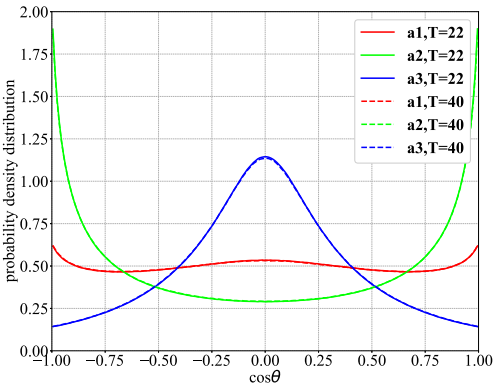

(d) Taylor scale

FIG. 14. Probability density function of the cosine of the angle between the vorticity vectors and the principle axes of strain rate tensor in different cases.

From the velocity field it is convenient to calculate the invariants of the rate of deformation tensor $\boldsymbol{A}$. The component of tensor $\boldsymbol{A}$ is defined as $a_{ij} = \partial \dot{x}_i / \partial x_j$. The invariants' distribution is sufficient to completely classify the topologies of the three-dimensional flow patterns [44]. The first-order differential equation of the velocity vector is [44]

$$\begin{bmatrix} u \\ v \\ w \end{bmatrix} = \begin{bmatrix} a_{11} & a_{12} & a_{13} \\ a_{21} & a_{22} & a_{23} \\ a_{31} & a_{32} & a_{33} \end{bmatrix} \begin{bmatrix} x \\ y \\ z \end{bmatrix}, \tag{24}$$

where u, v, w and x, y, z are the velocity and spatial coordinate components, respectively. The eigenvalues λ of the rate of deformation tensor $\boldsymbol{A}$ are determined by [44]

$$\det[\boldsymbol{A} - \lambda \boldsymbol{I}] = 0, \tag{25}$$

and the algebraic form is

$$\lambda^3 + P\lambda^2 + Q\lambda + R = 0. \tag{26}$$

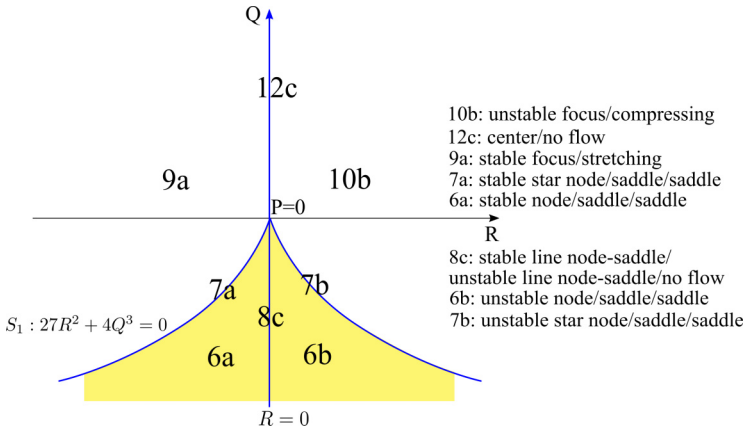

FIG. 15. Possible flow patterns in incompressible flows from Chong *et al.* [44].

According to Chong *et al.* [44], the canonical form of the invariants of the rate of deformation tensor $\boldsymbol{A}$ with Eq. (26) is

$$P = -(\lambda_1 + \lambda_2 + \lambda_3), \quad Q = \lambda_1\lambda_2 + \lambda_2\lambda_3 + \lambda_3\lambda_1, \quad R = -\lambda_1\lambda_2\lambda_3. \tag{27}$$

From the definition of P, Q, and R, their values can be further calculated from the components of the rate of deformation tensor $\boldsymbol{A}$ following the Einstein summation rule as [34]

$$P = -a_{ii}, \quad Q = -a_{ij}a_{ji}/2, \quad R = -a_{ij}a_{jk}a_{ki}/3. \tag{28}$$

As derived from Eq. (28), for the incompressible flows in this study, P is always 0. The R-Q plane fully depicts the turbulent flow patterns. The $R = 0$ line and curve $27/4R^2 + Q^3 = 0$ [34] divide the plane into four distinct pattern regions as shown in Fig. 15.

Figure 16 shows the R-Q scatter distribution of the gas (red) and liquid (blue) phases in the finite- and Taylor-scale simulations. For both phases, the flow pattern distribution is a teardrop shape and follows that of homogeneous isotropic turbulence in single gas phase flow. The dominant flow patterns are stable focus/stretching, unstable focus/compressing and unstable star node/saddle/saddle, which were explained in detail in Perry and Chong [45]. The R-Q distribution is more scattered in the gas phase at the initial stage of breakup for the large-scale cases because the deformation and spatial distribution of droplets are limited by inertial and surface tension. Large amounts of stable vortical flows are observed at this stage. With the breakup of droplets, the flow patterns generally become richer in both phases and the R-Q distribution reaches a similar state for all simulations. The flow field is modified, and the unstable tails become more significant with the generation of small-scale droplets. In this process, droplets deform and interact more quickly with the flow field. With the decrease of droplet scale, the initial condition for droplets is closer to that of the steady state, and the R-Q distribution looks similar at different times. The results for other droplet scales show the same trend and are not presented here for clarity.

The evolution of TKE of the whole flow field and the two phases are compared in Fig. 17. From the total TKE evolution, it is observed that the energy is first reduced after the adding of droplets except the Taylor-scale case. It is seen that the TKE is reduced to a larger extent with the decrease of initial droplet scale. This is because the more dispersed small-scale droplets have a more interacting area with the turbulence and therefore more effects on the total flow field. For the Taylor-scale case, droplets quickly obtain energy from the flow field, and therefore the total TKE level increases fast in both phases. The Taylor-scale case reaches equilibrium state and follows the TKE evolution of single-phase flow at the later time of simulation. The energy level in all simulations is increased and surpasses that of the single gas phase simulation after about a half of the breakup process, showing a higher level of turbulence in both phases. The larger scale cases obtain more TKE when the

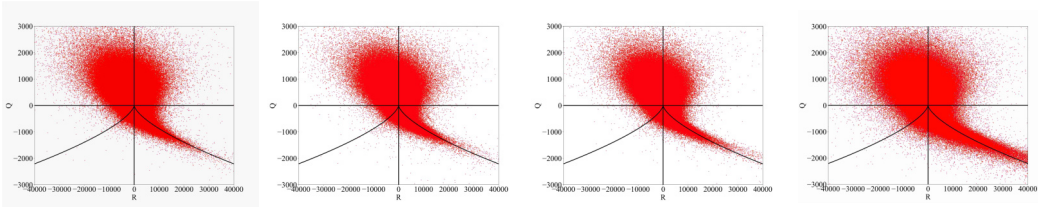

(a) T=22,finite (b) T=24,finite (c) T=26,finite (d) T=36,finite

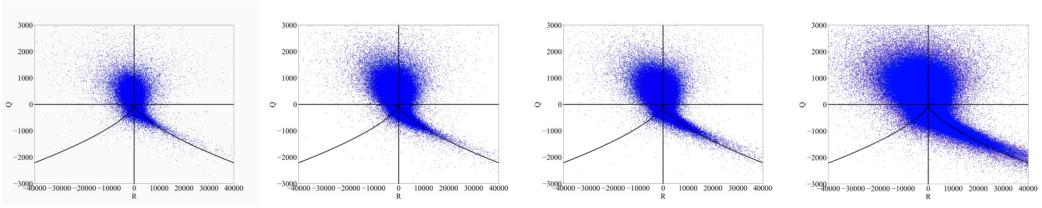

(e) T=22,finite (f) T=24,finite (g) T=26,finite (h) T=36,finite

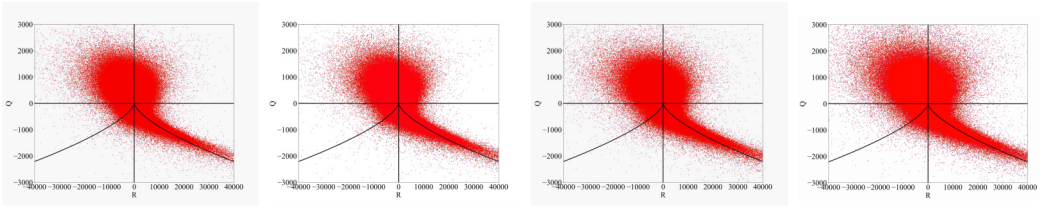

(i) T=22,Taylor (j) T=24,Taylor (k) T=26,Taylor (l) T=36,Taylor

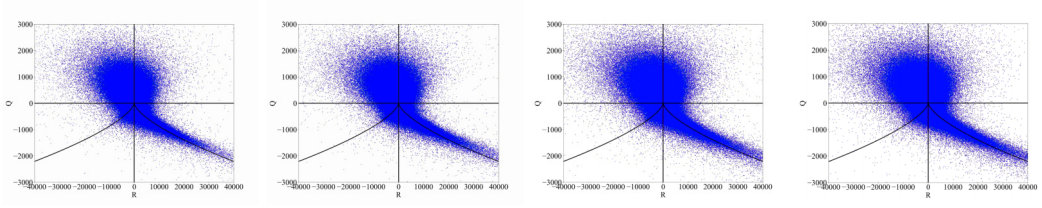

(m) T=22,Taylor (n) T=24,Taylor (o) T=26,Taylor (p) T=36,Taylor

FIG. 16. Scatters of *R*-*Q* invariant distribution. Red represents the gas flow field, and blue represents the liquid flow field.

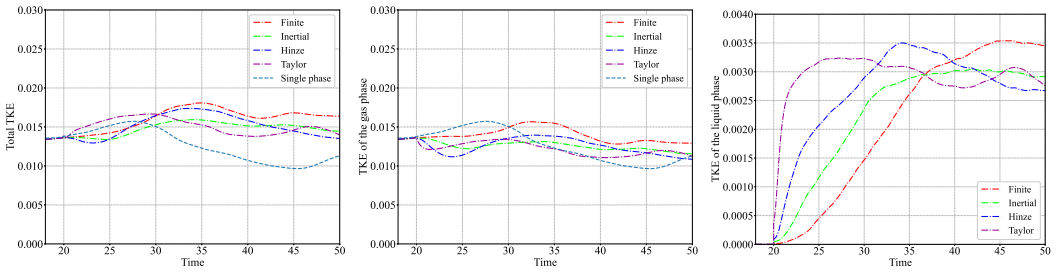

(a) Whole TKE (b) Gas TKE (c) Liquid TKE

FIG. 17. Evolution of TKE in the flow field.

continuous liquid phase deforms and absorbs energy from the flow field. Looking into the gas phase TKE, adding droplets reduces the TKE magnitude in the gas phase for all scale cases. The reduction effect increases with the decrease of initial droplet scale. This is because the scattered small droplets in the flow field break down the large structures of gas flow and induce more dissipation. Also shown in the figure is that the TKE magnitude restores more quickly for smaller scale cases due to their low inertia. At initial stage of breakup, the finite-scale case follows the single gas phase simulation better due to less effect on the whole gas field. The increase of TKE after $T = 28$ for large-scale cases is likely to be contributed by the breakup of continuous large-scale liquid structures. As the breakup proceeds, the fully developed Taylor-scale case follows the evolution of single gas phase flow better. The energy evolution of larger scale cases also follows the same trend and reaches a similar magnitude after $T = 40$. The TKE in the liquid phase is presented in Fig. 17(c). Small droplets respond quickly to the turbulent gas flow, and their TKE increases fast and reaches a steady state. The increase of coalescence probability can contribute to reducing the TKE in the Taylor- and Hinze-scale cases. With the increase of droplet scale, the TKE increase in the liquid phase is delayed to a larger extent. Due to the continuous energy input from linear forcing and the long breakup process, the TKE of larger droplets can reach a higher value. It is interesting to note that the gas and liquid TKE of the Hinze-scale case do not fall between the inertial- and Taylor-scale cases completely when breakup develops. The relatively middle-sized droplets absorb energy to a high level in the liquid phase at moderate rate, and the gas TKE also increases due to linear-forcing and perturbations, which shows a strong interaction between two phases.

IV. CONCLUSIONS

In this study, the interaction between droplets of a series of classical scales and homogeneous isotropic turbulence is investigated using numerical simulations. The effects on the motion and topological changes of the flow field are studied in detail and can help us to understand the droplet breakup mechanisms under realistic aeroengine combustor conditions. The main conclusions drawn from this paper are the following:

(1) The numerical strategy which combines LES with adaptive mesh refinement method is implemented and verified. It is shown to be capable of simulating relatively complex two-phase interaction with acceptable computational costs.

(2) Different scale droplets respond to the turbulent gas flow differently. With the decrease of initial droplet scale, they have less inertia to withstand the perturbations. Large-scale droplets experience periphery shedding and usually deform into a disklike shape before the final breakup. Due to the two-phase interaction, pressure perturbations are observed in the droplets and flow field. The average pressure of a flow field is 16 times at the steady state of breakup than the initial stage for the finite-scale case and increases 2.4 times for the small Taylor-scale simulation.

(3) The diameter probability density function reaches the similar state of unimodal distribution from different initial sizes. The SMD decreases to similar values around 0.01, and coalescence is observed. For the energy spectra,the energy for small-scale motions is increased and more fluctuations are shown in the inertial subrange.

(4) The existence and clustering of droplets can modify the vortical structure distribution in the flow field. Most vorticity vectors are aligned with the second eigenvector $\boldsymbol{a_2}$ of the strain rate tensor in all the cases.

(5) From the *R*-*Q* invariant scatters of the rate of deformation tensor, the flow patterns of the two phases are identified. The most common patterns in the flow field are stable focus/stretching, unstable focus/compressing, and unstable star node/saddle/saddle. In the process of breakup, the flow patterns become more diverse, and the unstable part is significantly increased.

(6) The evolution of turbulence kinetic energy are tracked and compared among different scales. It is shown that the TKE in the gas phase is initially suppressed due to the adding of droplets. The TKE of two-phase flow is larger in magnitude when the breakup fully develops. The smallest

Taylor-scale case absorbs energy quickly to increase the TKE and follows the single gas phase result due to low inertia.

ACKNOWLEDGMENTS

The research is conducted under the sponsorship from National Natural Science Foundation of China (No.11902267 and No.12272321). X.S. took part in the design and discussion of the study. He implemented the numerical simulations and analyzed the data. He wrote the original draft and did the editing and review work. H.Y. proposed the design and aims of the study. She reviewed the manuscript and helped to analyze the results and conclusions. F.C. proposed the design and aims of the study. He helped to analyze the results and conclusions.

[1] B.-F. Bai, H.-B. Zhang, L. Liu, and H.-J. Sun, Experimental study on turbulent mixing of spray droplets in crossflow, Exp. Therm Fluid Sci. **33**, 1012 (2009).

[2] H. Zhu, C. Pan, and H. Lian, Spatial correlations and relative velocities of polydisperse droplets in homogeneous isotropic turbulence, Phys. Fluids **34**, 083320 (2022).

[3] H. Wu, Z. Zhang, F. Zhang, K. Wu, and W. L. Roberts, Experimental estimation of turbulence modulation in droplet-laden two-phase jet, Phys. Rev. Fluids **8**, 094301 (2023).

[4] P. J. O'Rourke, Statistical properties and numerical implementation of a model for droplet dispersion in a turbulent gas, J. Comput. Phys. **83**, 345 (1989).

[5] P. Gualtieri, F. Battista, and C. M. Casciola, Turbulence modulation in heavy-loaded suspensions of tiny particles, Phys. Rev. Fluids **2**, 034304 (2017).

[6] M. S. Dodd and A. Ferrante, On the interaction of Taylor length scale size droplets and isotropic turbulence, J. Fluid Mech. **806**, 356 (2016).

[7] A. Roccon, M. De Paoli, F. Zonta, and A. Soldati, Viscosity-modulated breakup and coalescence of large drops in bounded turbulence, Phys. Rev. Fluids **2**, 083603 (2017).

[8] C. Shao, K. Luo, Y. Yang, and J. Fan, Direct numerical simulation of droplet breakup in homogeneous isotropic turbulence: The effect of the Weber number, Int. J. Multiphase Flow **107**, 263 (2018).

[9] P. K. Farsoiya, Z. Liu, A. Daiss, R. O. Fox, and L. Deike, Role of viscosity in turbulent drop break-up, J. Fluid Mech. **972**, A11 (2023).

[10] M. Gorokhovski and M. Herrmann, Modeling primary atomization, Annu. Rev. Fluid Mech. **40**, 343 (2008).

[11] D. Kim and P. Moin, Numerical simulation of the breakup of a round liquid jet by a coaxial flow of gas with a subgrid Lagrangian breakup model, *Annual Research Briefs* (Center for Turbulence Research, Stanford, CA, 2011).

[12] D. Fuster, A. Bagué, T. Boeck, L. Le Moyne, A. Leboissetier, S. Popinet, P. Ray, R. Scardovelli, and S. Zaleski, Simulation of primary atomization with an octree adaptive mesh refinement and VOF method, Int. J. Multiphase Flow **35**, 550 (2009).

[13] G. G. Agbaglah, Numerical study of hole formation in a thin flapping liquid sheet sheared by a fast gas stream, Phys. Fluids **33**, 062119 (2021).

[14] J. Smagorinsky, General circulation experiments with the primitive equations: I. The basic experiment, Mon. Weather Rev. **91**, 99 (1963).

[15] S. Elghobashi, Direct numerical simulation of turbulent flows laden with droplets or bubbles, Annu. Rev. Fluid Mech. **51**, 217 (2019).

[16] F. Xiao, M. Dianat, and J. J. McGuirk, LES of turbulent liquid jet primary breakup in turbulent coaxial air flow, Int. J. Multiphase Flow **60**, 103 (2014).

[17] D. Barreiro-Villaverde, A. Gosset, and M. A. Mendez, On the dynamics of jet wiping: Numerical simulations and modal analysis, Phys. Fluids **33**, 062114 (2021).

[18] S. Popinet, A quadtree-adaptive multigrid solver for the Serre–Green–Naghdi equations, J. Comput. Phys. **302**, 336 (2015).
[19] S. Popinet, An accurate adaptive solver for surface-tension-driven interfacial flows, J. Comput. Phys. **228**, 5838 (2009).
[20] J. A. van Hooft, S. Popinet, C. C. van Heerwaarden, S. J. van der Linden, S. R. de Roode, and B. J. van de Wiel, Towards adaptive grids for atmospheric boundary-layer simulations, Boundary Layer Meteorol. **167**, 421 (2018).
[21] C. W. Hirt and B. D. Nichols, Volume of fluid (VOF) method for the dynamics of free boundaries, J. Comput. Phys. **39**, 201 (1981).
[22] R. Scardovelli and S. Zaleski, Direct numerical simulation of free-surface and interfacial flow, Annu. Rev. Fluid Mech. **31**, 567 (1999).
[23] Y. Renardy and M. Renardy, Prost: A parabolic reconstruction of surface tension for the volume-of-fluid method, J. Comput. Phys. **183**, 400 (2002).
[24] S. B. Pope, *Turbulent Flows* (Cambridge University Press, Cambridge, 2000).
[25] A. N. Kolmogorov, The local structure of turbulence in incompressible viscous fluid for very large Reynolds numbers, Proc. R. Soc. London, Ser. A **434**, 9 (1991).
[26] D. K. Lilly, On the application of the eddy viscosity concept in the inertial sub-range of turbulence, *Volume 123 of NCAR manuscript: National Center for Atmospheric Research* (NCAR, 1966).
[27] M. Germano, U. Piomelli, P. Moin, and W. H. Cabot, A dynamic subgrid-scale eddy viscosity model, Phys. Fluids **3**, 1760 (1991).
[28] D. K. Lilly, A proposed modification of the Germano subgrid-scale closure method, Phys. Fluids **4**, 633 (1992).
[29] P. Moin and S. V. Apte, Large-eddy simulation of realistic gas turbine combustors, AIAA J. **44**, 698 (2006).
[30] X.-S. Tian, H. Zhao, H.-F. Liu, W.-F. Li, and J.-L. Xu, Three-dimensional large eddy simulation of round liquid jet primary breakup in coaxial gas flow using the VOF method, Fuel Process. Technol. **131**, 396 (2015).
[31] T. S. Lundgren, Linearly forced isotropic turbulence, *Annual Research Briefs* (Center for Turbulence Research, Stanford, CA, 2003).
[32] C. Rosales and C. Meneveau, Linear forcing in numerical simulations of isotropic turbulence: Physical space implementations and convergence properties, Phys. Fluids **17**, 095106 (2005).
[33] Y. Zhou and B. Thornber, A comparison of three approaches to compute the effective Reynolds number of the implicit large-eddy simulations, J. Fluids Eng. **138**, 070905 (2016).
[34] S. Mukherjee, A. Safdari, O. Shardt, S. Kenjereš, and H. E. Van den Akker, Droplet–turbulence interactions and quasi-equilibrium dynamics in turbulent emulsions, J. Fluid Mech. **878**, 221 (2019).
[35] F. Mashayek, Droplet–turbulence interactions in low-mach-number homogeneous shear two-phase flows, J. Fluid Mech. **367**, 163 (1998).
[36] R. J. Tabaczynski, Turbulence and turbulent combustion in spark-ignition engines, Prog. Energy Combust. Sci. **2**, 143 (1976).
[37] J. O. Hinze, Fundamentals of the hydrodynamic mechanism of splitting in dispersion processes, AIChE J. **1**, 289 (1955).
[38] R. Goldstein, K. Lau, and C. Leung, Velocity and turbulence measurements in combustion systems, Exp. Fluids **1**, 93 (1983).
[39] M. Heitor and J. Whitelaw, Velocity, temperature, and species characteristics of the flow in a gas-turbine combustor, Combust. Flame **64**, 1 (1986).
[40] S. Goebel, N. Abuaf, J. Lovett, and C.-P. Lee, Measurements of combustor velocity and turbulence profiles, in *Turbo Expo: Power for Land, Sea, and Air*, Vol. 78903 (American Society of Mechanical Engineers, 1993), p. V03AT15A079.
[41] M. Carl, T. Behrendt, C. Fleing, M. Frodermann, J. Heinze, C. Hassa, U. Meier, D. Wolff-Gaßmann, S. Hohmann, and N. Zarzalis, Experimental and numerical investigation of a planar combustor sector at realistic operating conditions, J. Eng. Gas Turbines Power **123**, 810 (2001).

[42] W. T. Ashurst, A. Kerstein, R. Kerr, and C. Gibson, Alignment of vorticity and scalar gradient with strain rate in simulated Navier–Stokes turbulence, Phys. Fluids **30**, 2343 (1987).

[43] B. Coriton and J. H. Frank, Experimental study of vorticity-strain rate interaction in turbulent partially premixed jet flames using tomographic particle image velocimetry, Phys. Fluids **28**, 025109 (2016).

[44] M. S. Chong, A. E. Perry, and B. J. Cantwell, A general classification of three-dimensional flow fields, Phys. Fluids **2**, 765 (1990).

[45] A. E. Perry and M. S. Chong, A description of eddying motions and flow patterns using critical-point concepts, Annu. Rev. Fluid Mech. **19**, 125 (1987).